

PAPER

[View Article Online](#)
[View Journal](#) | [View Issue](#)Cite this: *Catal. Sci. Technol.*, 2016,
6, 6916Received 20th May 2016,
Accepted 30th June 2016

DOI: 10.1039/c6cy01107a

www.rsc.org/catalysis

A DFT study of molecular adsorption on Au–Rh nanoalloys

Ilker Demiroglu,^a Z. Y. Li,^b Laurent Piccolo^c and Roy L. Johnston^{*a}

Density functional theory calculations are performed to investigate both mixing and adsorption properties of 38-atom and 79-atom Au–Rh nanoalloys at the nanoscale. The $\text{Rh}_{\text{core}}\text{Au}_{\text{shell}}$ and $\text{Rh}_{\text{ball}}\text{Au}_{\text{cup}}$ isomers are found to be energetically favourable with respect to other isomers. The adsorption strengths of reactive species such as H_2 , O_2 and CO are found to be greater on the Rh part than on the Au part of the nanoalloys and therefore a core–shell inversion is found to be feasible under a molecular environment. It is also found that underlying Rh atoms decrease the adsorption strength on the Au part whereas underlying Au atoms increase it on the Rh part of the nanoalloys. The strain, alloying and relaxation effects on adsorption strength are characterized using a sequential approach and their competing nature is demonstrated for the Au–Rh bimetallic system.

Introduction

At the nanoscale, catalytic as well as other properties of materials are often different from those of their bulk counterparts due to quantum size effects and geometric effects. In addition, since heterogeneous catalytic reactions take place on surfaces, nanoparticles are ideal catalysts due to their high surface/volume ratio. Moreover, they also possess a higher proportion of less-coordinated active sites. One example is gold, which in the bulk phase is catalytically inert for most heterogeneous reactions,¹ but which has been found to show exceptional catalytic properties toward CO oxidation and a number of other reactions for ultra-fine particles.²

Alloying different metals opens a way to achieve even greater potential for nanoparticles as catalysts, since additional structural motifs may enhance chemical and physical properties due to synergistic effects and properties can be tuned by varying composition and chemical ordering.³ Another advantage of multimetallic nanoalloys is the possibility of reducing the cost by mixing an efficient, but expensive catalyst—e.g. rhodium (Rh)—with another, cheaper metal without decreasing, or sometimes even improving catalytic performance.

The catalytic performance of multimetallic nanoalloys depends also on the chemical ordering in addition to the geom-

etry and size of the particles. In the literature it has been shown both theoretically and experimentally that binding ligands can change the chemical ordering or the structure of nanoparticles, thin films, and bulk surfaces.^{4–11} For example, Andersson *et al.* have shown that CO adsorption on a Cu–Pt near-surface alloy drives the less reactive Cu to the surface, although CO does not bind directly to the surface Cu.⁴ Tao *et al.* have shown that reversible core–shell inversion takes place for Pd–Rh nanoparticles depending on which molecules are chemisorbed and suggested that this behaviour can lead to the design of “smart catalysts” that may catalyse different reactions depending on the reaction environment.^{5,6} Theoretically, West *et al.* have studied the segregation patterns of several bimetallic couples such as Au–Pd, Pd–Pt, Cu–Pt, and Pd–Rh and presented a model for relating the changes in the chemical ordering of nanoalloys in reactive environments with metal–ligand interaction strengths.^{7,8}

Understanding metal–adsorbate interactions is important not only for determining the possible chemical ordering changes but also because adsorption is a key step in catalytic reactions. If reactive species are adsorbed too weakly, they may not be activated to undergo reaction, whereas if they are adsorbed too strongly, the desorption rate decreases and poisoning may occur (Sabatier’s principle). Metal–ligand interactions have been extensively studied for metal surfaces both experimentally and theoretically and the d-band model^{1,12,13} has been shown to be particularly useful in understanding bond formation and trends in reactivity. According to this model, the d-band centre of the metal surface or particle is used as a descriptor to anticipate metal–adsorbate interaction strength. It is known from the literature that upon alloying metals both strain^{14,15} and ligand^{16,17} effects can broaden or

^a School of Chemistry, University of Birmingham, Edgbaston, Birmingham B15 2TT, UK. E-mail: r.l.johnston@bham.ac.uk^b Nanoscale Physics Research Laboratory, School of Physics and Astronomy, University of Birmingham, Edgbaston, Birmingham B15 2TT, UK^c Institut de recherches sur la catalyse et l’environnement de Lyon (IRCELYON) UMR 5256 CNRS & Université Claude Bernard Lyon 1, 2 avenue Albert Einstein, F-69626 Villeurbanne, France

narrow the surface d-band and in turn change the position of the d-band centre, although it is difficult to separate these effects for extended surfaces.¹⁸ However, there are known exceptions to the d-band model, when the ligand has an almost completely filled valence shell and the metal surface has a nearly full d-band.¹⁹ One should be careful, both for nanoparticles and extended surfaces, since there also exist relaxation^{20,21} and/or reconstruction effects,^{22–24} which may be induced by adsorbates. Moreover, for nanoparticles, low-coordinated sites (corners and edges) also complicate the picture relative to the extended surfaces.²⁵

Rhodium is an important catalyst due to its efficiency in diverse reactions including hydrogenation, carbonylation, hydroformylation, and oxidation.²⁶ However it is scarce and expensive, therefore mixing with another metal which is more abundant and/or less expensive is desirable. Rhodium and gold are immiscible in the bulk,²⁷ however, alloying at nanoscale is possible but has been less extensively studied.^{28–34} Konuspayeva *et al.* synthesized *ca.* 3 nm sized Au–Rh bimetallic particles on well-defined rutile-titania nanorods by colloidal methods.²⁹ The authors reported that pre-calcination of Au–Rh nanoparticles mostly lead to separated Au and Rh nanoparticles, whereas pre-reduction generates a well-defined segregated structure with Rh located at the interface between Au and titania. With respect to Rh/TiO₂, the bimetallic catalyst exhibited improved resistance to air oxidation and to sulfidation during tetralin hydrogenation in the presence of H₂S. Moreover, AuRh/TiO₂ shows catalytic synergy for the hydrodeoxygenation of guaiacol.³⁵

In this work, we have investigated theoretically bimetallic Au–Rh clusters and the effect of adsorption of reactive species such as H₂, O₂ and CO. In the first section, we focus on mixing patterns of bare Au–Rh clusters. In the following three sections, we present our results on (i) H and H₂ adsorption, (ii) O and O₂ adsorption, and (iii) CO adsorption. In the fifth section, we compare adsorption results for different species and discuss the strain, alloying and relaxation effects on adsorption strength. In the last section, we move on to adsorption of multiple molecules and investigate the segregation patterns under different molecular environments.

Methodology

Though experimental catalysis studies have been performed on nanometre scale Au–Rh particles, DFT calculations are limited to clusters with a few tens or perhaps hundreds of atoms. In this study we have chosen to study 38-atom and 79-atom truncated octahedra (TO) clusters as models for bimetallic Au–Rh nanoparticles due to the high symmetry of the parent TO structure (O_h), and their fcc packing (as in the larger experimentally studied nanoparticles). While TO₃₈ is in the non-scalable region (*i.e.* where properties do not scale simply with cluster size), comparison with TO₇₉ (and in some cases with clusters with up to 260 atoms, see below) enable us to draw trends which we believe are applicable in the scal-

able region, thereby bridging the size gap to the experimental nanoparticles.

Initially, single-atom substitutions of Au in Rh and Rh in Au were investigated for 38- and 79-atom TO clusters for all the symmetrical positions shown in Fig. 1. Following the single atom substitutions, we have constructed several nanoalloy models covering different compositions and morphologies, such as core-shell and Janus particles (Fig. 2 shows examples for TO₃₈). Ordered alloy particles are generated by alternating layers of Au and Rh in the [100] or [111] directions and by occupying different fcc crystal positions with Au or Rh. To allow a comparison between bimetallic TO₃₈ clusters which have the same composition, surface-decorated configurations of Au₃₂Rh₆ (hex and centroid) as in the study of West *et al.*⁸ are also included in the set, together with the Rh_{core}Au_{shell} structure. The hex structure (h-Au₃₂Rh₆) has 6 Rh atoms forming a hexagonal ring surrounding one of the (111) facets of TO₃₈ (C_{3v} symmetry), while the centroid structure (c-Au₃₂Rh₆) has 6 Rh atoms occupying the centres of 6 of the (111) facets, with overall D_{3d} symmetry (see Fig. 2). Because of the impossibility of a perfect half and half Janus particle for the 79-atom TO, both Au- and Rh-rich Janus particles are studied together with “ball and cup” structures, in which one type of atom is embedded in the other but is not completely covered.³⁶ These general structural types are then expanded to larger (116-, 140-, 201-, and 260-atom) TO clusters to gain insight into clusters with sizes approaching those of real nanocatalysts.

Both atomic and molecular adsorptions of hydrogen, oxygen and CO molecules are studied on selected 38-atom TO structures. In single-atom adsorption studies, adsorbates are initially placed on all possible surface sites. According to these results, several adsorption configurations are studied for molecular adsorbates, including both atoms of the adsorbate bonding to the cluster *via* two metal atoms for O₂ adsorption, giving an M–O–O–M bridge, which is denoted $\mu_2\eta^2$ type bonding. $\mu_1\eta^1$ denotes one atom of the adsorbate connected to a metal atom on an atop position and $\mu_2\eta^1$ denotes adsorption of the adsorbate through one atom bridging two metal atoms (see Fig. 3). For multiple adsorbate studies of O₂ and CO molecules on TO₃₈ clusters, simpler atop positions on (111) facets are chosen to investigate trends for these higher symmetry systems. When a comparison is made for clusters of the same composition for adsorption of 6 molecules, the best

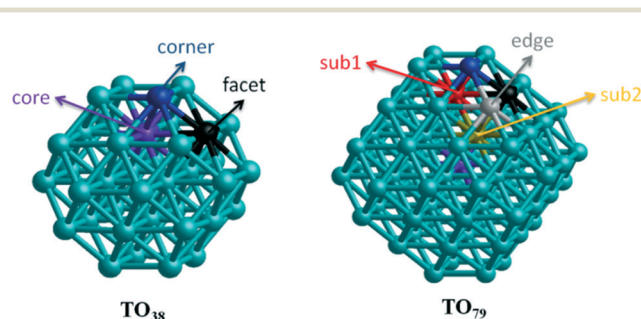


Fig. 1 Symmetrical positions on 38- and 79-atom TO cluster models.



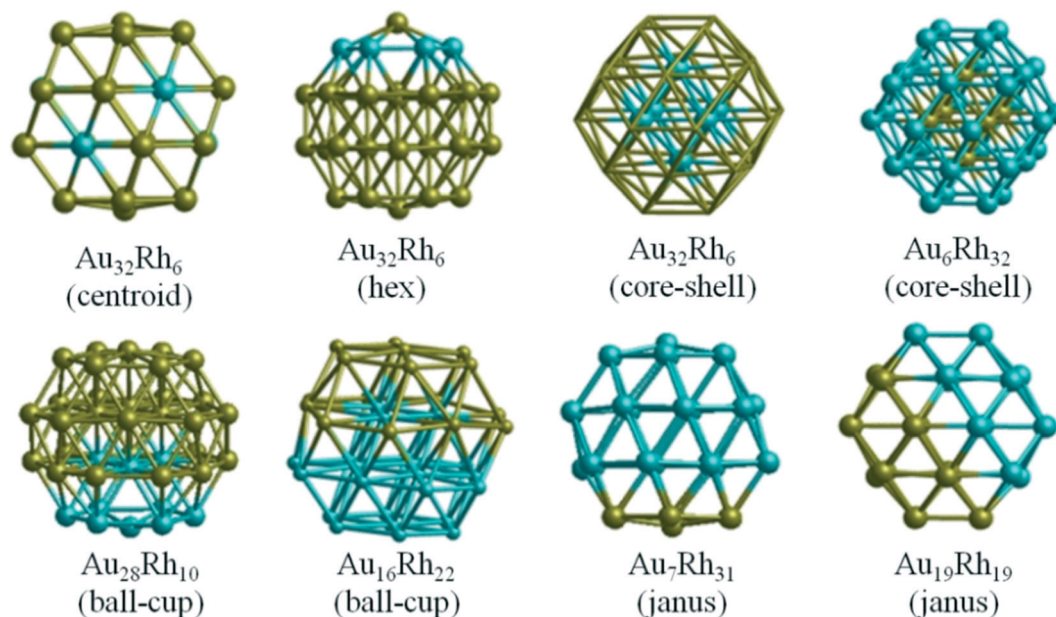


Fig. 2 38-atom TO Au-Rh nanoalloy models showing several compositions and chemical orderings. Blue spheres represent Rh atoms and yellow spheres represent Au atoms.

adsorption positions observed from single adsorbate considerations are also included and compared.

Calculations are performed using density functional theory (DFT) as implemented in the VASP³⁷ code. The generalized gradient approximation (GGA) was employed within the Perdew–Burke–Ernzerhof (PBE)³⁸ parameterization for the exchange–correlation energy functional. All the calculations are spin-polarized, with valence electrons treated explicitly (Rh: s^1d^8 , Au: s^1d^{10} , C: s^2p^2 , O: s^2p^4 , and H: s^1), while the ionic cores are represented by the projected augmented wave (PAW)^{39,40} method. To avoid spurious periodic interactions, unsupported clusters are placed into a sufficiently large supercell that ensures ~ 10 Å separation by vacuum. The Γ point is used to sample the Brillouin zone. For all of the bare clusters and clusters with adsorbed molecules, local geometry optimizations were performed, at the DFT level, where all atoms are relaxed until the forces on the atoms are lower than 0.01 eV Å⁻¹ and the electronic ground states are determined by requiring a total energy convergence of 10^{-6} eV. However, in section 5, to isolate the different effects contributing to the adsorption strength trends, partly or fully frozen

geometry calculations were also performed for comparison. Dissociation energy barriers for H₂ and O₂ molecules on nanoparticles were calculated using the nudged elastic band (NEB) method.^{41,42}

For the comparison of the energetics of different composition nanoalloys, a mixing energy term (Δ)⁴³ was calculated, which is expressed as:

$$\Delta = E_{\text{tot}}(A_mB_n) - m \frac{E_{\text{tot}}(A_{m+n})}{m+n} - n \frac{E_{\text{tot}}(B_{m+n})}{m+n} \quad (1)$$

where the total energy (E_{tot}) of the nanoalloy A_mB_n is compared to the pure metal clusters of A and B of the same size ($m+n$). Hence, a negative value of Δ means an energy decrease upon mixing and therefore favourable mixing.

Adsorption energy (E_{ads}) values are calculated as the differences in the total energies of the combined and separated systems:

$$E_{\text{ads}} = - (E_{\text{tot}}(\text{combined}) - E_{\text{tot}}(\text{cluster}) - E_{\text{tot}}(\text{adsorbate})) \quad (2)$$

For the H and O atom adsorptions, $E_{\text{tot}}(\text{adsorbate})$ values are taken as half of the total energies of H₂ and O₂ molecules, respectively. It should be noted that adsorption energies, E_{ads} , as defined in eqn (2), are negative quantities. In the following discussion, the terms “stronger adsorption” or “higher adsorption energy” will be used to refer to configurations with more negative values of E_{ads} , i.e. larger values of $|E_{\text{ads}}|$.

The d-band centre is calculated as:

$$d_{\text{centre}} = \frac{\int \rho E dE}{\int \rho dE} \quad (3)$$

where ρ is the d-band density, E is the d-band energy, ρdE is the number of states. d_{centre} values are calculated only for

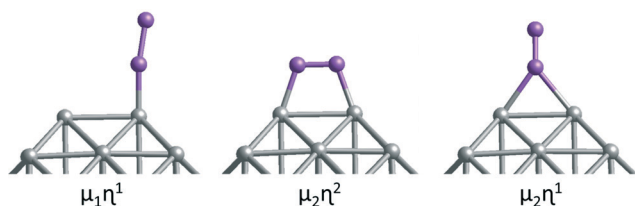


Fig. 3 Metal adsorbate bonding types. The symbol μ stands for the number of metal atoms to which the adsorbate binds and the symbol η stands for the number of atoms in the adsorbate which bind to the metal. Grey spheres represent metal atoms and purple spheres represent adsorbate atoms.



(111) facets of the clusters to allow a comparison between alloyed and pure clusters.

Results

1. Bare clusters

For TO_{38} , a Rh dopant preferentially occupies a core position, while facet and corner positions also have negative (favourable) mixing energies (see Fig. 1 and Table 1). Conversely the preference for a single Au dopant is corner > facet > core, all having positive (unfavourable) mixing energies. These findings are consistent with the higher cohesive energy of Rh compared to Au.³¹ Similarly, for the larger TO_{79} cluster, a Rh dopant is favoured in the core position followed by sub-surface positions, while surface Rh gives a positive mixing energy. In contrast, for a single Au dopant in TO_{79} , the stability order is corner > edge > facet > subsurface > core, with only the corner position giving a negative mixing energy. Table 2 summarises the mixing energy results for the addition of a second dopant, both connected to (adjacent) and far from the first dopant in TO_{38} . For both Au and Rh dopants, site preferences remain the same as for the first dopant, whether it is connected to the first dopant or not. However, while the Au dopants prefer to be connected to each other, Rh dopants prefer to be separate. This is because Rh dopants try to maximise the number of Au–Rh bonds as the strength of Rh–Au is greater than that of Au–Au bonds. As the strength of Rh–Au is lower than that of Rh–Rh bonds, Au dopants behave in the opposite fashion, to minimise disruption of Rh–Rh bonds by occupying adjacent positions.

Fig. 4a shows the variation of mixing energy (Δ) with composition and type of Au–Rh segregation for 38-atom TO clusters. As expected from single-atom substitution results, as shown in Table 1, the $\text{Rh}_{\text{core}}\text{Au}_{\text{shell}}$ isomer is the most stable configuration for all considered TO sizes, while the inverse $\text{Au}_{\text{core}}\text{Rh}_{\text{shell}}$ isomer is the least stable configuration. One can see from Fig. 4a that the mixing energies of the intermediate structures between core–shell and the corresponding pure metal particles lie on a straight line for both $\text{Rh}_{\text{core}}\text{Au}_{\text{shell}}$ and $\text{Au}_{\text{core}}\text{Rh}_{\text{shell}}$, where the core is partially filled with one atom type. When we swap one core Rh atom with a surface Au atom, the increase in energy is found to be 0.96 eV for facet positions, while it is 1.17–1.49 eV for corner positions. When we add another Rh atom on the surface of $\text{Rh}_{\text{core}}\text{Au}_{\text{shell}}$, it

Table 2 Mixing energy values (eV) for substitution of a second atom of Au into Rh and Rh into Au for 38-atom TO clusters. For each position of the first dopant the most stable position for the second dopant is indicated in bold font

First dopant	Core (adjacent)	Core (far)	Facet (adjacent)	Facet (far)	Corner (adjacent)	Corner (far)
$\text{Au}_2\text{Rh}_{36}$						
Core	3.58	3.80	2.24	2.41	1.72	1.91
Facet	2.24	2.41	—	1.04	0.57	0.53
Corner	1.72	1.91	0.57	0.53	0.02	0.16
$\text{Rh}_2\text{Au}_{36}$						
Core	−2.09	−2.21	−1.61	−1.60	−1.28	−1.33
Facet	−1.61	−1.60	—	−0.87	−0.65	−0.73
Corner	−1.28	−1.33	−0.65	−0.73	−0.37	−0.47

prefers facet over corner sites and the mixing energy values increase (the clusters are destabilised) by 0.32 eV and 0.58 eV, respectively.

For clusters with surface Rh and having the same composition ($\text{Au}_{32}\text{Rh}_6$) as $\text{Rh}_{\text{core}}\text{Au}_{\text{shell}}$, we have observed that corner sites ($\text{h-Au}_{32}\text{Rh}_6$; $\Delta = 1.10$ eV) are preferred over facet sites ($\text{c-Au}_{32}\text{Rh}_6$; $\Delta = 1.28$ eV) for Rh atoms, in contrast to single atom calculations and addition of a surface Rh atom on $\text{Rh}_{\text{core}}\text{Au}_{\text{shell}}$, where the additional Rh atom is more likely to occupy a facet site than a corner site. This is because the neighbouring Rh atoms stabilise each other due to the stronger Rh–Rh bonds, while the facet sites have isolated Rh atoms. Replacing the Au atom in the centre of the Rh_6 ring in the $\text{h-Au}_6\text{Rh}_{32}$ isomer leads to an Au-rich Janus-type structure ($\text{Au}_{31}\text{Rh}_7$) with a mixing energy of 1.41 eV while the regular Janus particle is found to have $\Delta = 1.20$ eV. At the Rh-rich side, the $\text{h-Au}_6\text{Rh}_{32}$ isomer ($\Delta = -0.25$ eV) is found to be more stable than $\text{c-Au}_6\text{Rh}_{32}$ and $\text{Au}_{\text{core}}\text{Rh}_{\text{shell}}$. Similarly the Rh-rich Janus structure is found to also have negative mixing energy (−0.09 eV) and is therefore more stable than the 50:50 Janus particle, whereas the Au-rich Janus particle is less stable. $\text{Rh}_{\text{ball}}\text{Au}_{\text{cup}}$ configuration is the second best structure type after $\text{Rh}_{\text{core}}\text{Au}_{\text{shell}}$ particles, with mixing energies of −0.87 eV for $\text{Au}_{28}\text{Rh}_{10}$ and −0.67 eV for $\text{Au}_{16}\text{Rh}_{22}$. However the inverse of these particles ($\text{Au}_{\text{ball}}\text{Rh}_{\text{cup}}$) is found to be less stable than the Janus particles, with mixing energies of 3.29 eV for $\text{Au}_{10}\text{Rh}_{28}$ and 4.73 eV for $\text{Au}_{22}\text{Rh}_{16}$. Similarly, ordered alloy clusters are found unstable. For the ordered L_{12} phase, mixing energies are 3.54 eV for $\text{Au}_8\text{Rh}_{30}$, 4.43 eV for $\text{Au}_{10}\text{Rh}_{28}$, 4.33 eV for $\text{Au}_{28}\text{Rh}_{10}$, and 2.01 eV for $\text{Au}_{30}\text{Rh}_8$. For alternating layers in the [100] direction (L_{11} phase), mixing energies are 4.67 eV for $\text{Au}_{18}\text{Rh}_{20}$ and 4.56 eV for $\text{Au}_{20}\text{Rh}_{18}$, while it is 4.35 eV for alternating layers in the [111] direction (L_{10} phase) for $\text{Au}_{19}\text{Rh}_{19}$.

To test that the isomer preferences observed for TO_{38} are applicable to larger clusters, we have compared the mixing energy per atom (Δ/n) as a function of composition and segregation type for TO clusters with 38, 79, 116, 140, 201 and 260 atoms. As shown in Fig. 4b, the stability order found for TO_{38} is maintained for TO_{79} , TO_{116} , TO_{140} , TO_{201} , and TO_{260} , with the configurations grouped in the ellipses. The general stability order is $\text{Rh}_{\text{core}}\text{Au}_{\text{shell}} > \text{Rh}_{\text{ball}}\text{Au}_{\text{cup}} > \text{Janus} > \text{AuRh}_{\text{ordered}} \approx$

Table 1 Mixing energy values (eV) for single-atom substitution of Au into Rh and Rh into Au for 38- and 79-atom TO clusters. For each composition the most stable arrangement is indicated in bold font

Site	$\text{Au}_1\text{Rh}_{37}$	$\text{Rh}_1\text{Au}_{37}$	$\text{Au}_1\text{Rh}_{78}$	$\text{Rh}_1\text{Au}_{78}$
Core	1.88	−1.13	2.14	−0.47
Facet	0.53	−0.64	0.24	0.38
Corner	0.10	−0.29	−0.21	0.76
Edge (79)	—	—	0.16	0.40
Sub1 (79)	—	—	1.65	−0.20
Sub2 (79)	—	—	1.69	0.03



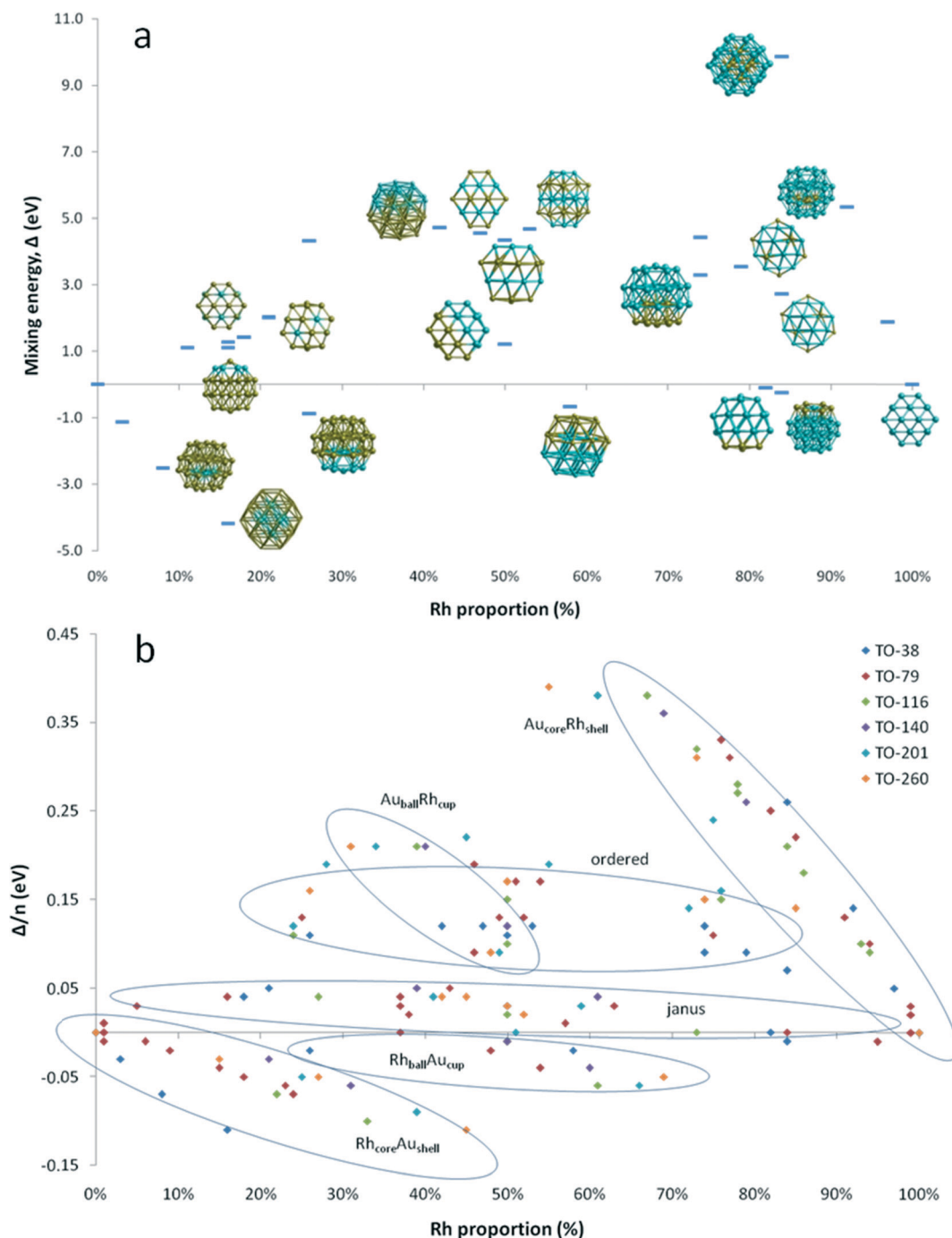


Fig. 4 (a) Mixing energy (Δ) versus atomic composition for 38-atom TO nanoalloys. Corresponding structures are shown. Blue spheres represent Rh atoms and yellow spheres represent Au atoms. (b) Mixing energy per atom (Δ/n) versus atomic composition for all considered TO sizes. Ellipses are a guide to eye.

$\text{Au}_{\text{ball}}\text{Rh}_{\text{cup}} > \text{Au}_{\text{core}}\text{Rh}_{\text{shell}}$, while only $\text{Rh}_{\text{core}}\text{Au}_{\text{shell}}$ and $\text{Rh}_{\text{ball}}\text{Au}_{\text{cup}}$ structures have negative mixing energies.

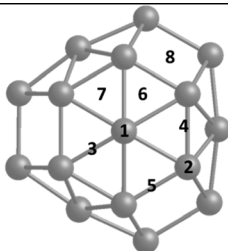
2. H and H_2 adsorption

Table 3 lists single H atom adsorption energies for all surface positions on both Au_{38} and Rh_{38} clusters. On Au_{38} the preferred position for adsorption of atomic H (*i.e.* the site with

the most negative E_{ads}) is the bridge position on the (111) facet, followed by the atop position on a corner atom of the (111) facet. On extended Au surfaces it has been reported that the preferred positions are the hollow sites (hcp and fcc sites are found to be degenerate) for Au(111) and the bridge site for Au(100), while the latter has a higher adsorption energy.⁴⁴ Unlike on the Au(111) surface, all H placements on hollow and four-fold positions on the Au_{38} cluster converged to



Table 3 Single atom adsorption sites on TO_{38} clusters and adsorption energies (eV) for H and O atoms on both Au_{38} and Rh_{38} clusters. The most favourable site for each cluster (most negative E_{ads}) is shown in bold while the calculations in which the H or O atoms spontaneously relaxed to other positions are greyed out

	Site	H–Au	H–Rh	O–Au	O–Rh
	1 (atop)	–0.05	–0.15	–1.07	–0.73
	2 (atop)	–0.23	–0.09	0.00	–1.54
	3 (bridge)	–0.29	–0.26	–1.09	–1.65
	4 (bridge)	–0.11	–0.57	–1.09	–1.98
	5 (bridge)	–0.19	–0.47	–1.07	–2.20
	6 (hcp-hollow)	–0.29	–0.28	–1.07	–1.96
	7 (fcc-hollow)	–0.29	–0.45	–1.09	–2.10
	8 (fourfold-hollow)	–0.19	–0.46	–0.81	–2.29

neighbouring bridge positions, probably because the corner atom of the (111) facet is no longer a true (111)-type surface atom, having a lower coordination number and therefore being more reactive, while the preference for the bridge site is in agreement with the extended Au(100) surface. On the Rh_{38} cluster the bridge positions at the edges are the favoured positions, followed by hollow positions in general. This is in agreement with extended surface studies, where the hollow sites are found to be preferred for Rh(111) and bridge and four-fold sites for the Rh(100) surface.⁶ On the Rh_{38} cluster, unlike Au_{38} , atop positions are found to be the least favourable for binding atomic hydrogen. The H atom adsorption energy on Rh_{38} is higher than on Au_{38} (by 0.28 eV when comparing the most preferable adsorption sites).

When we compare H atom results with H_2 molecule adsorption, Au atoms tend to have almost no interaction with H_2 molecules, while Rh readily dissociates H_2 . This is in agreement with previous theoretical study on Au_{13} ⁴⁵ cluster, in which the authors also reported no adsorption of H_2 molecules, whereas spontaneous H_2 dissociation was reported on Au_{14} and Au_{29} .⁴⁶ On Rh_{38} the dissociative adsorption energies of H_2 are consistent with the single H atom adsorptions. For example, for the lowest energy case, the H atoms migrate to two neighbouring bridge positions, with a total adsorption energy of –1.10 eV, which is only 0.04 eV lower than the sum of adsorption energies of two H atoms adsorbed on the corresponding sites (–0.57 and –0.47 eV). For the Au–Rh nanoalloys, the core–shell and Janus clusters are found to behave in the same way as the pure Au or Rh clusters, *i.e.* while there is almost no interaction on the Au part, spontaneous H_2 dissociation takes place on the Rh part of the corresponding clusters (see Fig. 5). H_2 dissociation is also observed for h- $\text{Au}_{32}\text{Rh}_6$ where there are neighbouring surface Rh atoms. The only case where the H_2 adsorption strength is found to be smaller than for pure Rh_{38} is for c- $\text{Au}_{32}\text{Rh}_6$, in which there are isolated Rh atoms on the cluster surface and the H_2 dissociates with the two H atoms remaining on the same Rh atom (H–H distance: 1.52 Å). There is a 0.5 eV energy barrier to migration onto another Rh atom *via* bonding to the Au atoms, however fully dissociated hydrogen (with the two H atoms on different Rh atoms) is less stable by 0.2 eV.

3. O and O_2 adsorption

Single O atom adsorption energies for all surface sites on Au_{38} and Rh_{38} clusters are given in Table 3. Unlike the single H atom, on the Au_{38} cluster hollow positions are found to be the preferred sites for O adsorption while bridge and atop positions are not favourable and converge to hollow sites. This is in agreement with the higher adsorption energies reported on Au(111), Au(211) and Au_{13} for hollow sites, while the bridge positions except for Au(211) diffused to other positions.⁴⁷ Similarly the fourfold hollow position was also found to be preferred on Rh_{38} , followed by bridge positions. This disagrees with a previous study, which reported the fourfold sites are the least stable on Rh(211) and Rh_{13} .⁴⁷ In the same study, it is reported that the fcc-hollow site is preferred on Rh(111), followed by the hcp-hollow, which correlates well with the higher adsorption energies for fcc- and hcp-hollow sites on Rh_{38} . Also in that study it was reported that bridge position is preferred on Rh(211), which correlates with the higher adsorption energies of bridge positions between lower-coordinated Rh atoms. Lastly, for Rh_{13} the threefold site is reported to be preferred, which we believe is because in Rh_{13} all three Rh atoms have low coordination, unlike in Rh_{38} , while the fourfold site is composed of low coordination Rh atoms. Consistent with the previous study,⁴⁷ in our work the atop positions have the lowest adsorption energies. For Rh_{38} , the atomic O adsorption energy is higher on Rh than on Au, with a 1.20 eV energy difference between the best adsorption sites considered.

Moving on to O_2 adsorption, again the Rh cluster tends to adsorb O_2 more strongly than the Au cluster (adsorption energies for best configurations: –2.41 eV (Rh) *vs.* –0.95 eV (Au)). This is in line with experimental studies which reported no adsorption for oxygen on clean Au(111) and Au(110) surfaces⁴⁸ whereas O_2 readily dissociates at low coverages on low index Rh surfaces.⁴⁹ However, adsorption of molecular O_2 has been shown to be possible on stretched Au(111),⁵⁰ Au(211)⁵⁰ and small Au nanoparticles,⁵¹ albeit with very weak binding energies.

The adsorption energy is lowest (least negative E_{ads}) for the atop position on a (111) facet of Au_{38} (only –0.19 eV), while for the atop position on an edge atom it is –0.49 eV.



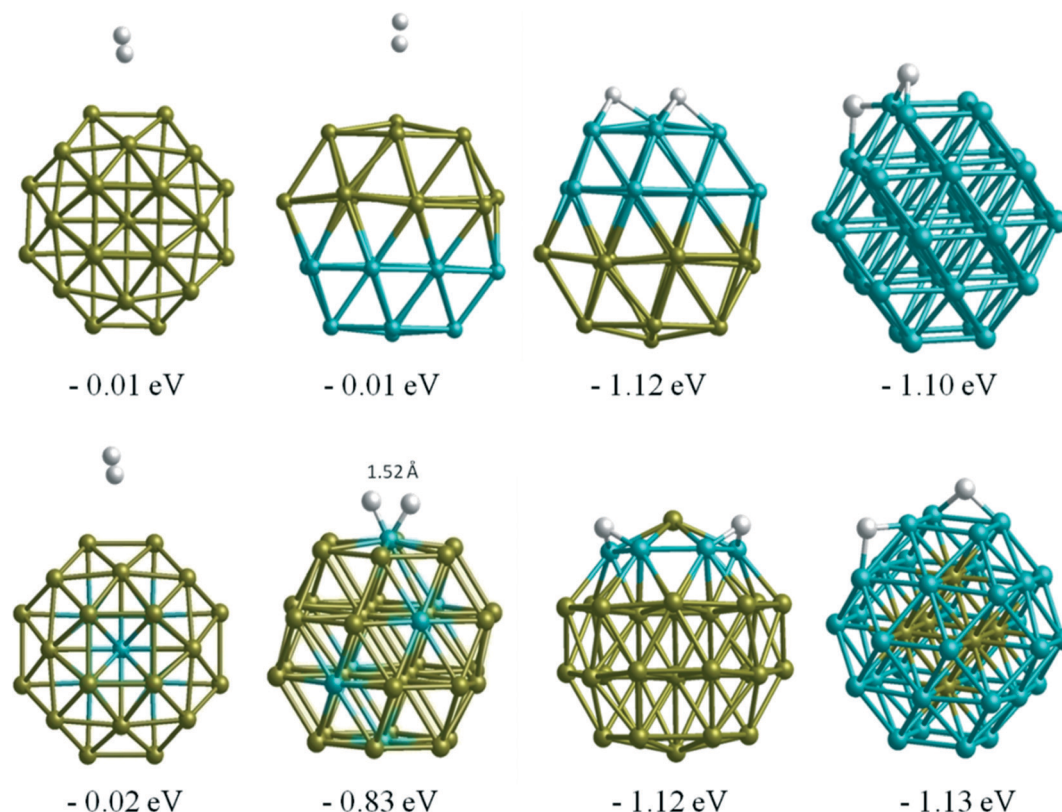


Fig. 5 H_2 molecule adsorption configurations and energies on TO_{38} clusters.

This difference is attributed to the edge atoms being more reactive due to having lower coordination numbers. The adsorption strength for the bridge positions on the (111) facet and the edge between two (111) facets of $\mu_2\eta^1$ type are found to be relatively weak (E_{ads} values are -0.26 and -0.27 eV, respectively) while for the bridge site between (111) and (100) facets it is found to be stronger (-0.56 eV) and is accompanied by a distortion, with the Au edge atoms moving apart from each other. The energetically best positions on the Au_{38} cluster are found for the $\mu_2\eta^2$ type bonding on the bridge positions. On the bridge site on (111) facet the adsorption energy is -0.64 eV, while (111)–(111) and (111)–(100) bridge sites have adsorption energies of -0.89 eV and -0.95 eV, respectively.

For Rh_{38} no local minima could be found for the atop positions since Rh interacts more strongly than Au with the O_2 molecule and therefore the second O atom spontaneously bonds to a neighbouring Rh atom to make a Rh–O–O–Rh bridge ($\mu_2\eta^2$ type). The adsorption energy for the $\mu_2\eta^2$ type bonding on the (111) facet is -1.71 eV while on the (111)–(111) bridge it is -2.41 eV. Similar to the atop positions, starting from $\mu_2\eta^1$ type bonding on the bridge sites no local minima were located, with the O_2 molecules dissociating spontaneously.

To determine the effect of alloying on O_2 adsorption, we compared several adsorption geometries corresponding to those on the pure Au and Rh clusters (see Table 4). For all clusters $\mu_2\eta^2$ type binding is found the most favourable,

mainly on the bridge site between two (111) facets. For pure Au and on the Au side of Janus particles (Janus-Au), O_2 adsorption on the bridge site between (111) and (100) facets is slightly lower in energy than between two (111) facets due to adsorbate-induced relaxation. The Au–Au distance of the (111)–(111) bridge site increases by 0.26 Å upon O_2 adsorption while the Au–Au distance for the (111)–(100) bridge increases by 0.48 Å. Similarly, the Au–Au elongations are 0.22 Å for the (111)–(111) bridge versus 0.62 Å for the (111)–(100) bridge for Janus-Au. However, for the $\text{Rh}_{\text{core}}\text{Au}_{\text{shell}}$ particle, the Rh core limits this Au–Au bond elongation and the bridge bond elongation values are lowered to 0.18 Å for (111)–(111) versus 0.14 Å for (111)–(100). Therefore adsorption energies are increased and O_2 adsorption on the (111)–(111) bridge is favoured over the (111)–(100) bridge.

For $\text{c-Au}_{32}\text{Rh}_6$, the preference for $\mu_2\eta^2$ binding is less pronounced since the O_2 molecule prefers to bind to Rh atoms rather than Au and there is no possibility for $\mu_2\eta^2$ binding through two Rh atoms. Hence, $\mu_2\eta^2$ bridging between Rh and Au on the (111) facet (E_{ads} : -0.98 eV) is significantly more favourable than other $\mu_2\eta^2$ positions (E_{ads} : -0.45 eV and -0.05 eV). Very similar energies are found for $\mu_2\eta^1$ bridging between Rh and Au on (111) facets (E_{ads} : -0.94 eV) and the $\mu_1\eta^1$ atop site on Rh (E_{ads} : -0.93 eV). When the O_2 molecule binds only to Au atoms on $\text{c-Au}_{32}\text{Rh}_6$, adsorption energies are significantly reduced (less negative): the adsorption energy is only -0.15 eV for the $\mu_1\eta^1$ atop binding on an edge Au atom, -0.14 eV for the $\mu_2\eta^1$ bridge between two Au atoms and -0.45



Table 4 Adsorption energy values (eV) for O₂ molecule adsorption on 38-atom TO structures. The best configuration for each structure (most negative E_{ads}) is shown in bold font, while the calculations in which the O₂ molecule spontaneously dissociated or relaxed to other positions are greyed out

Site	Type	Position	Au ₃₈	Rh _{core} Au _{shell}	c-Au ₃₂ Rh ₆	h-Au ₃₂ Rh ₆	Janus-Au	Janus-Rh	Au _{core} Rh _{shell}	Rh ₃₈
Atop	$\mu_1\eta^1$	Centre of facet	-0.19	-0.03	-0.93	-0.10	-0.07	-2.01	-1.80	-1.71
		Edge of facet	-0.49	-0.11	-0.15	-1.34	-0.19	-2.54	-2.64	-2.41
Bridge	$\mu_2\eta^1$	Between two (111) facets	-0.27	-0.04	-0.03	-1.21	-0.09	-1.26	-1.33	-3.09
		Between (111) and (100) facets	-0.56	-0.04	-0.14	-1.25	-0.04	-1.40	-4.49	-4.44
		On (111) facet	-0.26	-0.02	-0.94	-1.21	-0.06	-1.09	-3.71	-4.00
Bridge	$\mu_2\eta^2$	Between two (111) facets	-0.89	-0.12	-0.04	-2.43	-0.27	-2.54	-2.64	-2.41
		Between (111) and (100) facets	-0.95	-0.05	-0.45	-2.38	-0.31	-2.51	-2.39	-3.17
		On (111) facet	-0.64	-0.03	-0.98	-1.04	-0.09	-2.01	-1.80	-1.71

eV for the $\mu_2\eta^2$ bridge between two Au atoms. Adsorption on these sites is 0.34 eV, 0.42 eV and 0.50 eV less favourable, respectively, than for the same sites on the pure Au₃₈ cluster.

For h-Au₃₂Rh₆, when the O₂ molecule is bound to the (111) Au atom at the centre of the Rh₆ hexagon, the adsorption energy (-0.10 eV) is lower than atop adsorption on the (111) facet of the pure Au₃₈ cluster (-0.19 eV). Similarly, when O₂ is bound across a Rh-Au bond in a $\mu_2\eta^2$ bridge, the adsorption strength is reduced relative to that on pure Rh₃₈ (-1.04 eV vs. -1.71 eV, respectively). However if the O₂ molecule is bound to two Rh atoms, in the same position as on the pure Rh cluster, the adsorption energy increases slightly, by 0.02 eV.

For O₂ adsorption on Rh_{core}Au_{shell}, we observe a very weak Au-O₂ interaction, with a highest adsorption energy of -0.12 eV for the $\mu_2\eta^2$ bridge between two (111) facets. For all positions the adsorption energies are significantly lower than on pure Au. In the reverse case, for the Au_{core}Rh_{shell}, atop positions spontaneously relax to $\mu_2\eta^2$ bridge sites *via* O binding to a neighbouring Rh atom, as for the pure Rh case. Conversely, the adsorption energies for O₂ on Au_{core}Rh_{shell} are -1.80 eV for the $\mu_2\eta^2$ bridge on the (111) facet and -2.64 eV for the (111)-(111) bridge site, which are 0.09 and 0.23 eV higher than for pure Rh₃₈. Similarly, adsorption energies on the Rh side of the Janus particle (Janus-Rh) are also greater than for pure Rh₃₈. However, in this case the adsorption strength enhancement is greater for the $\mu_2\eta^2$ bridge site on the (111) facet than for the (111)-(111) bridge site, with increases of 0.30 and 0.13 eV, respectively.

Comparing molecular O₂ adsorptions with the separate adsorptions of two O atoms on the best adsorption sites, for both Au and Rh dissociated O₂ is thermodynamically more favourable than molecularly adsorbed O₂ (see Fig. 6). For a comparison between Au, Rh, Janus and core-shell structures, we have calculated the energy barriers for O₂ dissociation on the same site (bridge $\mu_2\eta^2$ site between two (111) facets) on clusters. The barrier is calculated to be 0.12 eV on Rh₃₈ and 1.53 eV on Au₃₈. When we compare the energy barriers for Au₃₈ with the Rh_{core}Au_{shell} and Janus-Au ones, it increases to 2.04 eV and 1.82 eV, respectively. On the contrary, the energy barriers for Au_{core}Rh_{shell} and Janus-Rh decrease relative to the Rh₃₈, to become almost zero (0.02 eV). These very low energy barriers on the Rh part also explain why O₂ dissociates spontaneously on the $\mu_2\eta^1$ bridge sites for most Rh and Au_{core}Rh_{shell} particles, since for O₂ $\mu_2\eta^1$ binding is less favourable than $\mu_2\eta^2$.

In order to determine to what extent the results obtained for the 38-atom clusters can be extended to larger clusters, we have performed calculations for O₂ adsorption on the larger 79-atom TO clusters. We found the same adsorption sites to be the most favourable ones on TO₇₉ as on TO₃₈. For the Au₇₉ cluster, $\mu_2\eta^2$ type binding on the (111)-(100) bridge site has the highest adsorption energy (-0.37 eV), which is considerably weaker than on the Au₃₈ cluster (E_{ads} = -0.95 eV). This is consistent with the fact that molecular adsorption on large Au nanoparticles and extended Au surfaces is weaker than on small Au clusters.^{50,52} For Rh₇₉, $\mu_2\eta^2$ type binding to the

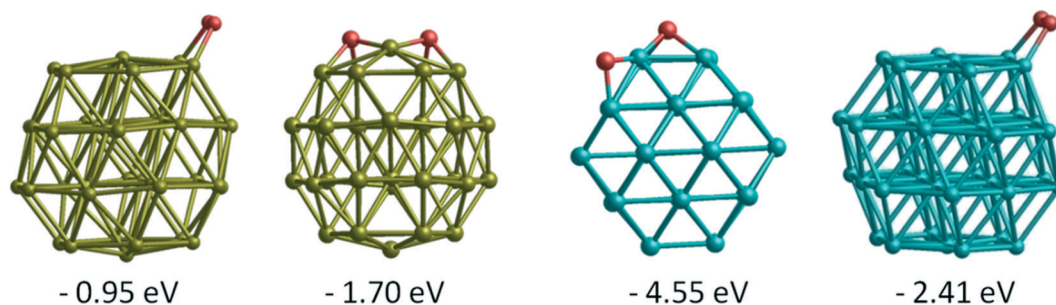


Fig. 6 Adsorption energies and structures of both molecular and dissociated O₂ on Au₃₈ and Rh₃₈ clusters.



(111)–(111) bridge site has the highest adsorption energy (–2.40 eV), which is same as for the Rh_{38} cluster. For Rh_{38} , some starting positions for the O_2 molecule on Rh_{79} resulted in O_2 dissociation. For the alloyed particles, we see the same adsorption energy trends as in 38-atom TO clusters. For the $\text{Rh}_{\text{core}}\text{Au}_{\text{shell}}$ cluster ($\text{Au}_{19}\text{Rh}_{60}$), the CO adsorption energy increases relative to pure Rh_{79} by 0.28 eV due to the underlying Au core atoms. On the other hand, the adsorption energy of CO on the $\text{Au}_{\text{core}}\text{Rh}_{\text{shell}}$ cluster ($\text{Au}_{60}\text{Rh}_{19}$) decreases slightly relative to the pure Au_{79} case by 0.09 eV because of the underlying Rh core atoms.

4. CO adsorption

Similar to the O_2 adsorption case, CO adsorbs more strongly on Rh_{38} than Au_{38} , with adsorption energies of –2.15 eV and –1.12 eV, respectively for the best adsorption sites. On the Au nanocluster, CO atop adsorption and $\mu_2\eta^1$ type binding on the (111) facet induce a spontaneous step formation on the (111) facet where the adsorbate binds, as shown in Fig. 7. This behaviour is consistent with experimentally observed CO-induced step-edge roughening on Au(111) surfaces.^{53,54} For Au_{38} , the adsorption is stronger if the CO molecule binds in an atop position on the edge of a (111) facet instead of the centre of the (111) facet and the bridge positions ($\mu_2\eta^1$ binding). In contrast to the Au cluster, $\mu_2\eta^1$ binding on the (111)–(111) bridge site is preferred for Rh_{38} .

In a previous study, CO adsorption energies for atop and bridge sites on the Au(111) surface were reported as –0.02 and 0.06 eV, respectively, while the adsorption energies were found to be increased on the step on the Au(211) surface, with the atop site still being slightly preferable over bridge positions (E_{ads} : –0.32 and –0.31 eV, respectively).⁴⁷ The site preferences are in agreement with our results, while the adsorption energies differ by ~ 0.7 eV because of the extra reac-

tivity of Au nanoparticles reported in the same study. The adsorption energy of CO on Au_{13} was also reported as –0.88 eV, which is similar to our values. For CO adsorption on Rh surfaces, while the atop site was preferred on Rh(111), the bridge site was favoured on the Rh(211) step (E_{ads} : –1.55 and –1.67 eV, respectively).⁴⁷ This is also in agreement with our results since the atop site on the edge of the (111) facet is preferred over the atop site on the (111) facet itself, due to the lower-coordinated edge atoms. Similarly, adsorption on the bridge site on the (111) facet is less favourable, while the bridge sites between facets are preferred since they represent the more reactive step edge. Although on Rh_{13} the threefold hollow site is reported to be preferred over bridge sites,⁴⁷ we believe that this is again because all the Rh atoms in the threefold hollow site have low-coordination numbers, unlike Rh_{38} . When we placed CO on a threefold site of Rh_{38} , it migrated to the bridge site between two low coordinated Rh atoms.

Moving to the Au–Rh nanoalloys, similar trends are observed as for O_2 adsorption, where the underlying Au or Rh layers affect the adsorption strength in opposite ways. As can be seen in Fig. 7, the adsorption strength is lower on Janus-Au than on Au_{38} , due to the underlying Rh atoms, while CO-induced step formation is also hindered, possibly due to the strain induced by the lattice mismatch between Rh and Au. In the reverse scenario, where the CO adsorbs on Janus-Rh, generally the adsorption strength increases relative to the pure Rh case (see Table 5). While the $\mu_2\eta^1$ bridge site is preferred on pure Rh, the atop position on the (111) facet becomes the favoured adsorption site on Janus-Rh.

Unlike O_2 adsorption, where the O_2 molecule tends to bridge two surface atoms, the CO molecule prefers to bind to the surface through only the carbon atom ($\mu_1\eta^1$ or $\mu_2\eta^1$). Thus, c- $\text{Au}_{32}\text{Rh}_6$, which has isolated Rh atoms on the cluster

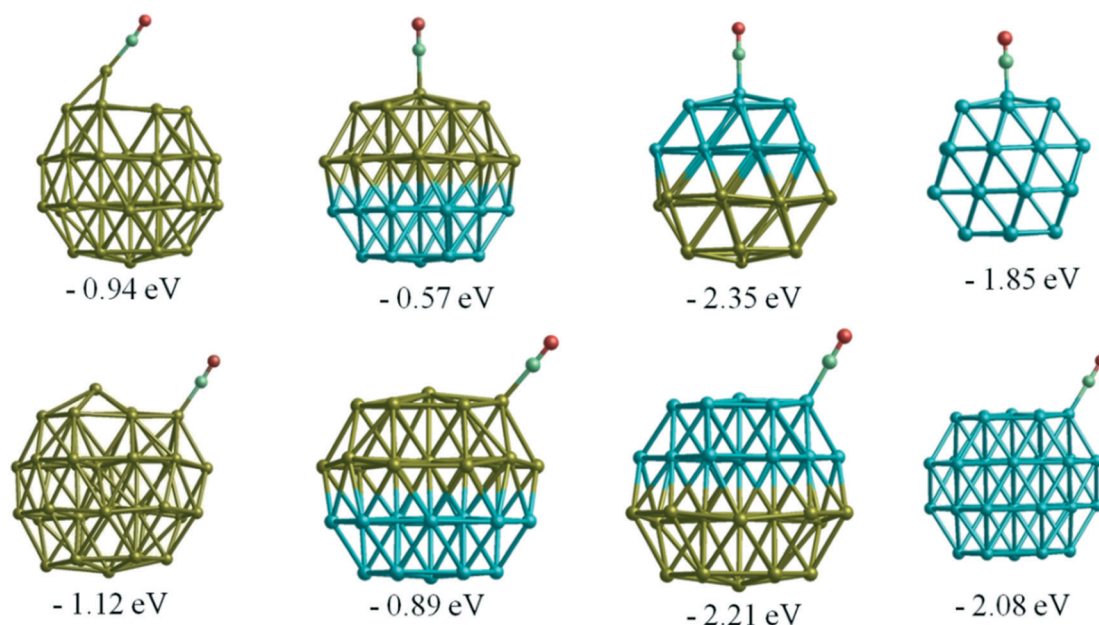


Fig. 7 CO adsorption in atop positions on Au, Rh, and Janus clusters. Adsorption energies are given in eV.



Table 5 Adsorption energy values (eV) for CO molecule adsorption on 38-atom TO structures. The best configuration for each structure (most negative E_{ads}) is shown in bold font while the calculations which spontaneously converged to other configurations are greyed out

Site	Type	Position	Au ₃₈	Rh _{core} Au _{shell}	c-Au ₃₂ Rh ₆	h-Au ₃₂ Rh ₆	Janus-Au	Janus-Rh	Au _{core} Rh _{shell}	Rh ₃₈
Atop	$\mu_1\eta^1$	Centre of facet	-0.94	-0.24	-2.32	-0.59	-0.55	-2.33	-2.04	-1.85
		Edge of facet	-1.12	-0.85	-0.87	-2.36	-0.87	-2.19	-2.20	-2.08
Bridge	$\mu_2\eta^1$	Between two (111) facets	-0.96	-0.48	-0.88	-2.31	-0.83	-2.13	-2.34	-2.15
		Between (111) and (100) facets	-1.10	-0.27	-0.88	-2.47	-0.81	-2.31	-2.25	-2.08
		On (111) facet	-1.10	-0.85	-2.32	-2.36	-0.71	-2.11	-2.13	-1.82

surface also shows stronger CO adsorption than the pure Rh cluster for the same atop configuration, while exhibiting weaker adsorption on the Au sides of the clusters for the atop and $\mu_2\eta^1$ type bridge positions, even weaker than on pure Au. When the CO molecule is placed in a bridging site between Au and Rh atoms it spontaneously converges to an atop Rh site for both c-Au₃₂Rh₆ and h-Au₃₂Rh₆. For h-Au₃₂Rh₆, the most favoured adsorption position is the $\mu_2\eta^1$ (111)–(100) Rh–Rh bridge position followed by the atop position on an edge Rh atom and the $\mu_2\eta^1$ (111)–(111) bridge site, respectively.

Similar to the Janus cluster, the adsorption strength of CO on the Rh_{core}Au_{shell} particle is lowered relative to the pure Au cluster, and the best adsorption site is found to be the atop position as in the pure Au cluster (see Table 4). The reduction of the adsorption strength is generally higher for the Rh_{core}Au_{shell} cluster than for the Janus-Au cluster. In the reverse case, for the Au_{core}Rh_{shell} cluster, the adsorption is again stronger than pure Rh while the same position is found to be the most favourable adsorption site. In contrast to CO binding on Au in the presence of Rh, the enhancement in the adsorption strength relative to pure Rh₃₈ for Au_{core}Rh_{shell} and the Janus-Rh structures varies for different positions, *e.g.* the adsorption strength for Janus-Rh is higher than Au_{core}Rh_{shell} for the atop position at the centre of the facet, while it is lower for the $\mu_2\eta^1$ (111)–(111) bridge position.

When we compare CO adsorption on the 38-atom TO clusters with adsorption on the larger 79-atom TO clusters, we observe similar trends between adsorption sites. For Au₇₉, the $\mu_1\eta^1$ atop site has the highest adsorption energy (–0.93 eV), which is close to the value of –1.12 eV for Au₃₈. $\mu_2\eta^1$ CO adsorption on the (111)–(100) bridge site and on the (111) facet has adsorption energies of –0.78 eV and –0.73 eV, respectively. For Rh₇₉, $\mu_1\eta^1$ binding on the atop site and $\mu_2\eta^1$ binding on the (111) facet have very similar adsorption energies of –2.23 eV and –2.22 eV, respectively. These values are slightly larger than the values for Rh₃₈ (–2.08 eV and –2.15 eV, respectively). For the alloyed particles, we see the same adsorption energy trends as for 38-atom TO clusters. For the Rh_{core}Au_{shell} cluster (Au₁₉Rh₆₀), the CO adsorption energy increases relative to pure Rh₇₉ by 0.25 eV due to the underlying Au core atoms. On the other hand, the adsorption energy of CO on Au_{core}Rh_{shell} (Au₆₀Rh₁₉) decreases slightly relative to pure Au₇₉ by 0.09 eV because of the underlying Rh core atoms.

5. Alloying effect on adsorption strength

When we consider the molecular adsorption studies discussed above, one striking effect is that the adsorption strength on one particular metal (Au or Rh) is affected by the presence of the other metal, whether it is in direct contact with the adsorbing metal atom or not. For both CO and O₂ adsorptions on the Au part of the clusters, in general the adsorption strength decreases relative to the pure Au case when there are underlying Rh atoms, as in the Janus-Au and Rh@Au core–shell cases, even though for Janus-Au the underlying Rh atoms are not in direct contact with the surface Au atoms to which the molecules are adsorbed. For the reverse situation, where there are Au atoms underneath the Rh surface atoms, the strength of molecular adsorption increases relative to the pure Rh case. Fig. 8 shows the relationship between the CO and O₂ adsorption energies and the d-band centres of the clusters. According to the d-band model, an upshift in the d-band centre should correlate with higher adsorption strength. However, when we compare the d-band centres of Janus-Au and Rh_{core}Au_{shell} clusters with pure Au, we observe a significant upshift for both, although the adsorption strength decreases. When we compare the d-band centres of Janus-Rh and Au_{core}Rh_{shell} clusters with pure Rh, there is an upshift for Au_{core}Rh_{shell} while there is a downshift for Janus-Rh, although the adsorption strength increases for both. According to the graph, it is clear that only Au, Rh and Au_{core}Rh_{shell} clusters follow the relation, while there is deviation for adsorption on Janus-Rh. It is also interesting that for adsorption on the Au side of Janus and Rh_{core}Au_{shell} clusters we see the opposite relation between the adsorption strength and the d-band-centre position, *i.e.* the adsorption strength decreases while there is an upshift in the d-band centre.

To understand whether these deviations are due to the mechanical effect of structural relaxation or to electronic effects caused by alloying, adsorption calculations were performed for the same sites for fixed (frozen) clusters in a sequential approach. Firstly, to isolate the strain effect caused by alloying, we relax the bare alloy clusters and calculate adsorption energies on these clusters as if they were pure parent (Au or Rh) clusters by fixing their coordinates. Secondly, to isolate the electronic effect we calculate the corresponding adsorption energies for fixed alloy clusters. Lastly, we also optimise the cluster coordinates to obtain final adsorbate-induced relaxations on alloy and pure clusters, as shown in Fig. 9.



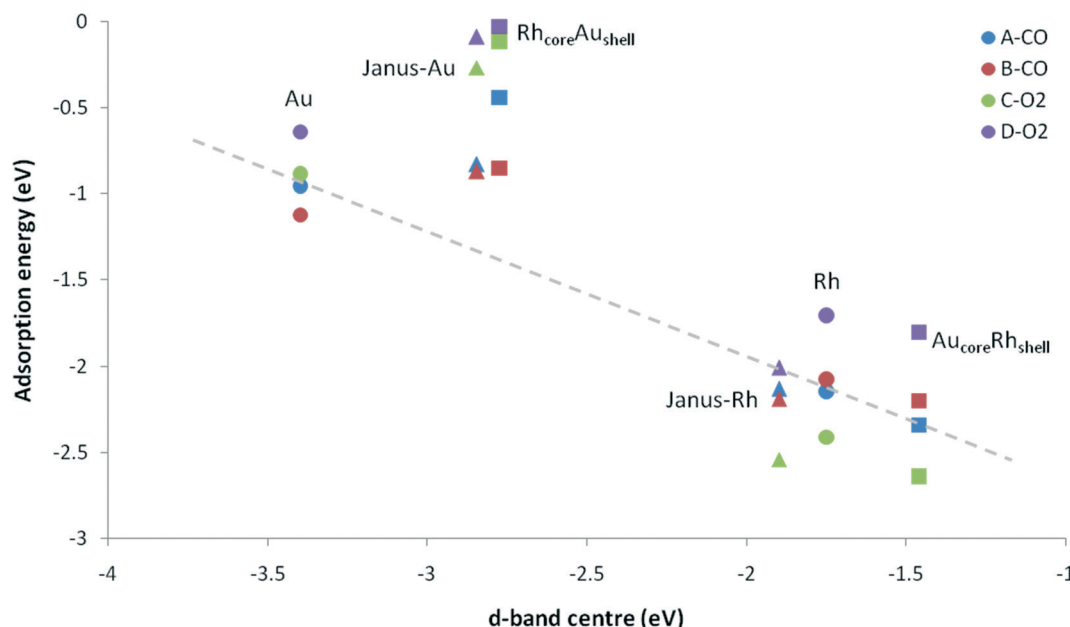


Fig. 8 Adsorption energy versus d-band centre for CO and O₂ adsorption on Au, Rh, Au_{core}Rh_{shell}, Rh_{core}Au_{shell}, and Janus particles. Circles, squares and triangles represent adsorption on pure, core-shell and Janus particles. A-CO, B-CO, C-O₂ and D-O₂ denote $\mu_2\eta^1$ (111)–(111), $\mu_1\eta^1$ corner, $\mu_2\eta^2$ (111)–(111), and $\mu_2\eta^2$ (111) adsorption sites, respectively. The dashed line is a guide for the eye.

For CO adsorption on both Janus-Rh and Au_{core}Rh_{shell}, the adsorption strength increases relative to pure Rh. However there is a downshift of the d-band centre in Janus-Rh whereas there is an upshift for Au_{core}Rh_{shell}. For Janus-Rh, when the competing effects are separated (see Fig. 9a), the alloying effect was found to lower the adsorption strength as expected, while the strain and relaxation effects strengthen the adsorption. As the strain and alloying effects are both due to the Au–Rh interface, the main reason for the higher adsorption energy as compared to pure Rh is the relaxation effect for CO adsorption on Janus-Rh. For CO adsorption on Au_{core}Rh_{shell} the strain and alloying effects reinforce each other, strengthening the adsorption while the strain effect is stronger for $\mu_2\eta^1$ (111)–(111) and the alloying effect is stronger for $\mu_1\eta^1$ type binding. This is because in $\mu_2\eta^1$ binding two Rh atoms are involved and the change of their bond length becomes dominant, whereas in $\mu_1\eta^1$ bonding the electronic effect on a single Rh atom is more important.

For O₂ adsorption on Janus-Rh (see Fig. 9c), as for CO adsorption, strain and alloying effects act in opposing directions and the strain effect for $\mu_2\eta^2$ (111)–(111) is less than for $\mu_2\eta^2$ (111) since in the latter case the central atom in the (111) facet is affected more by the strain (0.05 Å bond elongation) than the bridge position between two facets (0.02 Å bond elongation). The possible reason why the strain and alloying effects act in opposite senses is that the Au atoms are not connected directly to the adsorbing Rh atoms, hence they enhance the adsorption strength mainly because the Rh is stretched (strained) due to the Au–Rh size mismatch. For O₂ adsorption on Au_{core}Rh_{shell}, surprisingly the alloying effect also weakens the adsorption strength for $\mu_2\eta^2$ (111) binding although there is an upshift in the d-band centre, whereas

adsorption is strengthened, as expected, for $\mu_2\eta^2$ (111)–(111). This is because the strain is responsible for the upshift in d-band centre (which increases from –1.748 eV to –1.406 eV), while upon alloying there is a slight downshift (decreased from –1.406 to –1.461 eV). Strain and alloying effects together strengthen O₂ adsorption for both positions on Au_{core}Rh_{shell}.

On the Au side of the particles, the picture becomes more complicated. For CO $\mu_1\eta^1$ binding to a corner atom, the strain effect slightly weakens the adsorption while the alloying effect slightly strengthens it for both Janus-Au and Rh_{core}Au_{shell}, and the main reason for the stronger adsorption on pure Au seems to be the relaxation effect. For CO $\mu_2\eta^1$ (111)–(111) binding, however, the adsorption strength decreases both *via* the strain and alloying effects on Rh_{core}Au_{shell}, whereas they both strengthen the adsorption on Janus-Au. For O₂ adsorption on both Rh_{core}Au_{shell} and Janus-Au, the alloying effect always weakens the adsorption, unlike for CO adsorption. This behaviour is in agreement with the exception to the d-band model previously suggested for Pt and Pd, where the authors claimed that there is a repulsion between metal d-band and the molecule when alloying nearly fully occupied d⁹ or d¹⁰ metals with more electropositive metals, leading to opposite behaviour when the adsorbate has a completely filled valence shell.¹⁹ The weakening of the adsorption for both Janus-Au and Rh_{core}Au_{shell} is also accompanied by a reduced charge transfer to the molecule, similar to the $\mu_2\eta^1$ (111)–(111) CO adsorption case on Rh_{core}Au_{shell} (see Table 6). The charge transfer to the O₂ molecule is –0.63 for $\mu_2\eta^2$ (111) and –0.61 for $\mu_2\eta^2$ (111)–(111) on pure Au. However, charge transfer decreases to –0.43 and –0.37 for $\mu_2\eta^2$ (111) and –0.38 and –0.07 for $\mu_2\eta^2$ (111)–(111) on Janus-Au and Rh_{core}Au_{shell}, respectively. For the $\mu_2\eta^1$ (111)–(111) CO



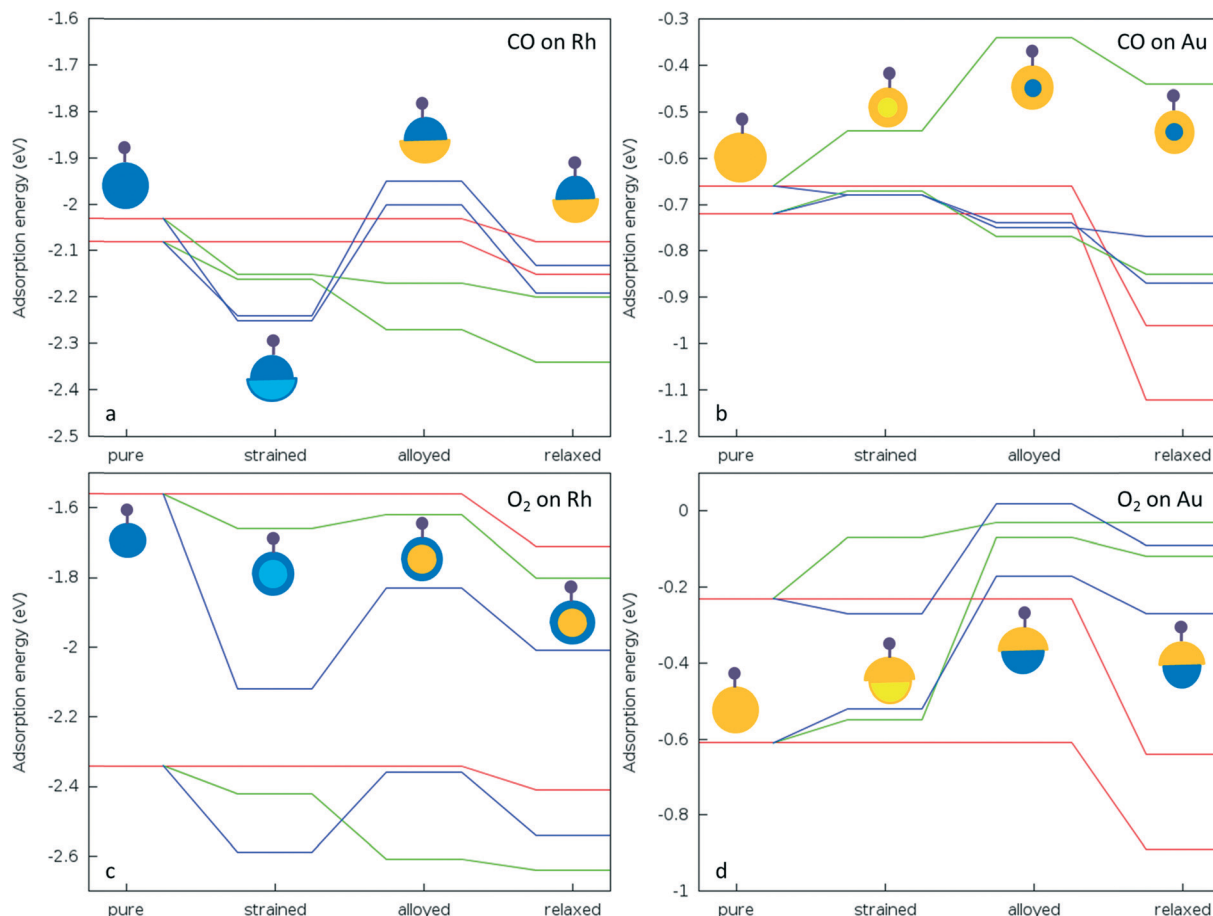


Fig. 9 Schematic view of the adsorption energy values for a) CO adsorption on Rh side, b) CO adsorption on Au side, c) O₂ adsorption on Rh side, and d) O₂ adsorption on Au side of the strained, alloyed and fully relaxed clusters with respect to their pure counterparts. Red lines represent pure clusters, blue lines represent Janus, and green lines represent core-shell clusters. For the illustrative pictures, blue represents Rh and yellow represents Au parts of the clusters. For the strained clusters light yellow (blue) represent the replaced Au (Rh) atoms on the coordinates of the Rh (Au) atoms as in alloyed structures. Adsorbate molecules are represented by the small ball-and-stick.

adsorption case, charge transfer decrease to the CO is 0.06 on Rh_{core}Au_{shell} than on pure Au, which explains the out of order behaviour of $\mu_2\eta^1(111)-(111)$ on Rh_{core}Au_{shell} with respect to Janus-Au and $\mu_2\eta^1(111)$ Rh_{core}Au_{shell} (see Fig. 9b).

Charge effects also play a role in the increase or decrease of adsorption strength on alloy clusters relative to their pure metal counterparts. For example, for both Janus-Rh and Au_{core}Rh_{shell} clusters the Rh layer charges become less negative (or even positive) than for pure Rh when alloyed with more electronegative Au atoms (see Table 6), which enhances the σ -donation from the adsorbate to the cluster. For Janus-Au and Rh_{core}Au_{shell} clusters, Au layer charges becomes more negative when alloyed with Rh, which reduces the σ -donation from the adsorbate to the cluster. However, charge effects alone cannot explain the extent of the change in the adsorption strength on alloying.

6. Multiple CO and O₂ adsorption

As mentioned above, for bare clusters Rh_{core}Au_{shell} is the energetically most favourable isomer. However, in adsorption studies, this isomer has the lowest adsorption strength to-

wards all adsorbates, even with respect to pure Au. Considering also that both CO and O₂ adsorption strengths on Rh are much higher than on Au, adsorption of multiple CO or O₂ molecules can potentially change the stability ordering of nanoalloy clusters,⁹ *i.e.* can stabilise surface Rh atoms.

Table 7 summarises the adsorption energy per O₂ molecule ($E_{\text{ads}}/\text{O}_2$) for the 38-atom TO nanoalloy clusters. The general adsorption trend is unchanged on increasing the number of adsorbates for most of the structures in terms of adsorption energy per number of adsorbates. An exception is the inverse core-shell structure (Au_{core}Rh_{shell}), for which we observe significant distortions such as Au migration to the surface and spontaneous O₂ dissociation during the initial computation stage. However, it should be noted that the Au_{core}Rh_{shell} structure was already the least stable structure among all of the considered nanoalloy morphologies, with a high mixing energy of ~ 10 eV and therefore prone to reconstruction. The $E_{\text{ads}}/\text{O}_2$ values also start to decrease for h-Au₃₂Rh₆, Janus and c-Au₃₂Rh₆ configurations after adsorption of 3, 4, and 8 molecules, respectively. This is because beyond these numbers the additional O₂ molecules have to



Table 6 Calculated d-band centres (eV) and charges on the (111) layer of bare TO_{38} clusters together with charge transfer to the adsorbate, metal-adsorbate and adsorbate-adsorbate distances, and adsorption energy values for CO and O_2 . A-CO denotes the adsorption type $\mu_2\eta^1$ (111)-(111), B-CO denotes $\mu_1\eta^1$ corner, C- O_2 denotes $\mu_2\eta^2$ (111)-(111), and D- O_2 denotes $\mu_2\eta^2$ (111)

Cluster	d-centre	Layer charge	Charge transfer	$d_{\text{C-O}}$	$d_{\text{M-C}}$	E_{ads}
A-CO						
Pure-Au	-3.399	-0.130	-0.180	1.178	2.121	0.960
$\text{Rh}_{\text{core}}\text{Au}_{\text{shell}}$	-2.772	-0.360	-0.120	1.169	2.133	0.440
Janus-Au	-2.844	-0.350	-0.160	1.174	2.107	0.830
Janus-Rh	-1.897	0.010	-0.410	1.188	2.007	2.130
$\text{Au}_{\text{core}}\text{Rh}_{\text{shell}}$	-1.461	-0.020	-0.420	1.191	1.988	2.340
Pure-Rh	-1.748	-0.260	-0.430	1.192	1.992	2.150
B-CO						
Pure-Au	-3.399	-0.130	-0.020	1.152	1.947	1.120
$\text{Rh}_{\text{core}}\text{Au}_{\text{shell}}$	-2.772	-0.360	-0.030	1.153	1.966	0.850
Janus-Au	-2.844	-0.350	-0.030	1.153	1.951	0.870
Janus-Rh	-1.897	0.010	-0.300	1.170	1.828	2.190
$\text{Au}_{\text{core}}\text{Rh}_{\text{shell}}$	-1.461	-0.020	-0.360	1.172	1.812	2.200
Pure-Rh	-1.748	-0.260	-0.330	1.171	1.836	2.080
Cluster	d-centre	Layer charge	Charge transfer	$d_{\text{O-O}}$	$d_{\text{M-O}}$	E_{ads}
C- O_2						
Pure-Au	-3.399	-0.130	-0.610	1.361	2.126	0.890
$\text{Rh}_{\text{core}}\text{Au}_{\text{shell}}$	-2.772	-0.360	-0.370	1.296	2.315	0.120
Janus-Au	-2.844	-0.350	-0.430	1.316	2.247	0.270
Janus-Rh	-1.897	0.010	-0.780	1.421	1.897	2.540
$\text{Au}_{\text{core}}\text{Rh}_{\text{shell}}$	-1.461	-0.020	-0.970	1.633	1.815	2.640
Pure-Rh	-1.748	-0.260	-0.770	1.403	1.910	2.410
D- O_2						
Pure-Au	-3.399	-0.130	-0.630	1.360	2.120–2.133	0.640
$\text{Rh}_{\text{core}}\text{Au}_{\text{shell}}$	-2.772	-0.360	-0.070	1.237	3.378–3.980	0.030
Janus-Au	-2.844	-0.350	-0.380	1.297	2.331–2.387	0.090
Janus-Rh	-1.897	0.010	-0.760	1.403	1.934–1.957	2.010
$\text{Au}_{\text{core}}\text{Rh}_{\text{shell}}$	-1.461	-0.020	-0.790	1.416	1.922–1.934	1.800
Pure-Rh	-1.748	-0.260	-0.780	1.407	1.931–1.987	1.710

bind to Au atoms rather than Rh atoms, due to the distribution of the Rh atoms.

When we compare the clusters of the same composition ($\text{Au}_{32}\text{Rh}_6$), where the $\text{Rh}_{\text{core}}\text{Au}_{\text{shell}}$ structure was the most favoured structure for the bare clusters, we find that adsorption of 6 O_2 molecules changes the stability orderings, with h- $\text{Au}_{32}\text{Rh}_6$ becoming the most stable (see Fig. 10). The c- $\text{Au}_{32}\text{Rh}_6$ isomer also slightly surpasses $\text{Rh}_{\text{core}}\text{Au}_{\text{shell}}$, however it is still 4.27 eV higher in energy than h- $\text{Au}_{32}\text{Rh}_6$.

As in the O_2 adsorption case, we also systematically compared multiple CO adsorption for all the nanoalloy structures (see Table 8). Following the step formation on the pure Au

cluster, we observed that multiple CO adsorption distorts the Au cluster drastically after adsorption of 2 CO molecules. For the $\text{Rh}_{\text{core}}\text{Au}_{\text{shell}}$ cluster, since the Rh core holds the Au shell more rigidly, distortions only start after 6–8 CO molecules, while for h- $\text{Au}_{32}\text{Rh}_6$, where all the Rh atoms lie around a single (111) facet, distortions are already seen for fewer CO adsorbates. Most of the distortions show the characteristic step formation as in the case of 1 CO molecule on the pure Au cluster.

Similar to the O_2 adsorption case, we have also observed that multiple CO adsorption changes the stability ordering of the $\text{Au}_{32}\text{Rh}_6$ clusters. While $\text{Rh}_{\text{core}}\text{Au}_{\text{shell}}$ is the lowest energy structure for bare clusters, the surface Rh-containing c- $\text{Au}_{32}\text{Rh}_6$ and h- $\text{Au}_{32}\text{Rh}_6$ structures become lower in energy than the core-shell particle upon adsorption of 6 CO molecules (see Fig. 10). In contrast to the O_2 case, the c- $\text{Au}_{32}\text{Rh}_6$ structure becomes slightly more favoured due to each CO molecule binding to one metal atom on the surface in a $\mu_1\eta^1$ fashion. However, the $\text{Rh}_{\text{core}}\text{Au}_{\text{shell}}$ isomer still lies 3 eV higher in energy.

Considering that surface Rh-containing c- $\text{Au}_{32}\text{Rh}_6$ and h- $\text{Au}_{32}\text{Rh}_6$ structures become more stable than $\text{Rh}_{\text{core}}\text{Au}_{\text{shell}}$ upon multiple molecular adsorption, we have also studied if one adsorbate can favour diffusion of Rh to the surface of the particle. To swap one core Rh atom to a surface position costs approximately 1 eV. However, when we adsorb one CO or O_2 molecule on that site, we end up with an isomer which is 0.41 eV lower in energy for CO adsorption and 0.11 higher in energy for O_2 adsorption. For O_2 adsorption this is expected, as O_2 prefers to bind to the surface through two surface Rh atoms. Displacing another Rh atom to the surface of the cluster is 0.34 eV lower in energy than for $\text{Rh}_{\text{core}}\text{Au}_{\text{shell}}$ (see Fig. 11). Together these suggest that total core-shell inversion is possible, though the segregation patterns are different for CO and O_2 . For O_2 adsorption, Rh atoms first prefer to occupy neighbouring corner sites which enable a stronger interaction with O_2 molecules, while for CO adsorption higher coordinated centroid sites are favoured for Rh atoms.

Conclusions

Nanoscale mixing properties of Au–Rh, preferred adsorption sites of small molecules and the effect of adsorption on Au–Rh segregation have been investigated using first-principles DFT calculations. In agreement with the higher cohesive and surface energies of Rh with respect to Au,⁵⁵ $\text{Rh}_{\text{core}}\text{Au}_{\text{shell}}$

Table 7 Adsorption energies (eV) for multiple O_2 adsorption on Au–Rh nanoalloys

# O_2	Au_{38}	$\text{Rh}_{\text{core}}\text{Au}_{\text{shell}}$	c- $\text{Au}_{32}\text{Rh}_6$	h- $\text{Au}_{32}\text{Rh}_6$	Janus	$\text{Au}_{\text{core}}\text{Rh}_{\text{shell}}$	Rh_{38}
1	-0.19	-0.02	-0.37	-0.93	-2.03	-1.70	-1.71
2	-0.12	-0.00	—	-1.01	—	-2.41	-1.80
3	-0.09	-0.00	-0.14	—	-1.95	-1.87	-1.77
4	-0.10	-0.00	-0.12	-0.99	-1.47	-3.22	-1.86
6	-0.08	-0.01	-0.08	-0.98	—	-3.67	-1.77
8	-0.16	-0.00	-0.07	-0.72	-0.98	-3.06	-1.87



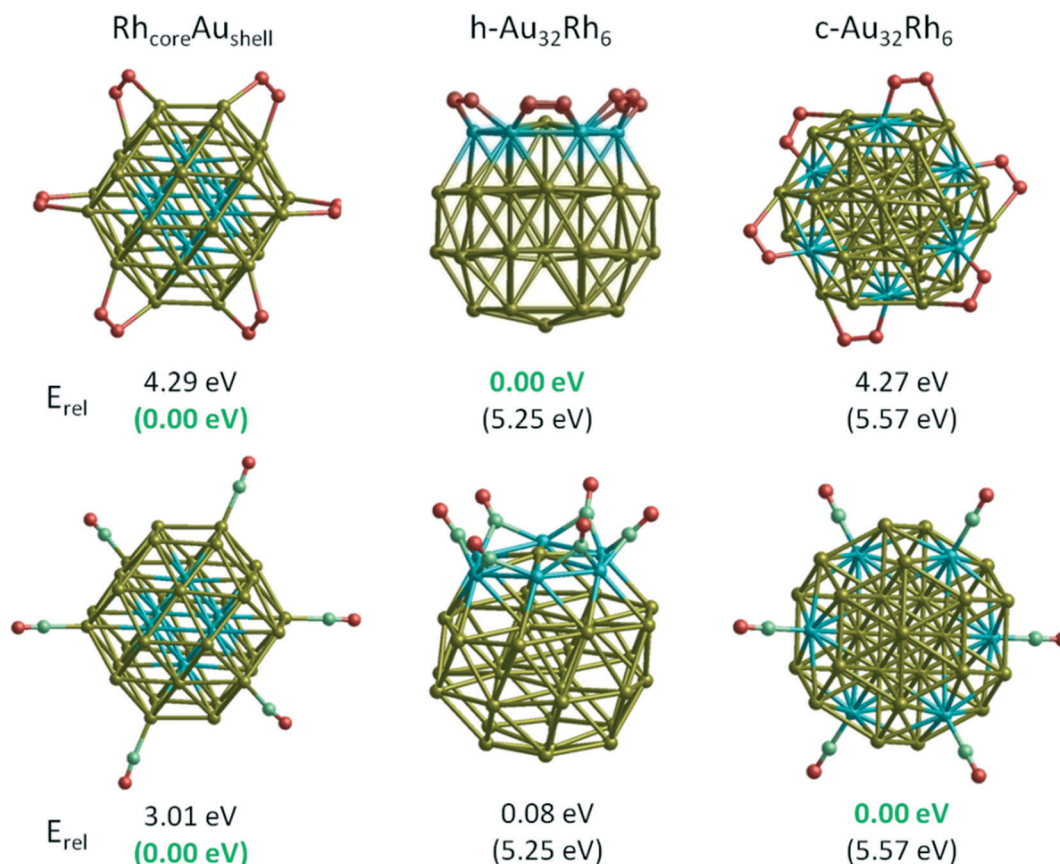


Fig. 10 Stability ordering change of $\text{Au}_{32}\text{Rh}_6$ cluster upon adsorption of 6 O_2 and 6 CO molecules. E_{rel} is the energy relative to the $\text{Rh}_{\text{core}}\text{Au}_{\text{shell}}$ isomer. Numbers in parentheses show the relative energies without O_2 molecules.

Table 8 Adsorption energies (eV) for multiple CO adsorption on Au–Rh nanoalloys

# CO	Au_{38}	$\text{Rh}_{\text{core}}\text{Au}_{\text{shell}}$	$\text{c-Au}_{32}\text{Rh}_6$	$\text{h-Au}_{32}\text{Rh}_6$	Janus	$\text{Au}_{\text{core}}\text{Rh}_{\text{shell}}$	Rh_{38}
1	−0.94	−0.14	−0.86	−2.32	−2.35	−1.94	−1.85
2	−1.20	−0.09	—	−2.29	—	−2.03	−1.89
3	−1.30	−0.23	−0.99	—	−2.30	−2.03	−2.04
4	−1.16	−0.25	−0.88	−2.28	−1.80	−2.05	−2.09
6	−0.98	−0.78	−0.89	−2.27	—	−2.09	−2.05
8	−1.00	−0.81	−1.07	−1.81	−1.41	−2.09	−2.08

clusters are found to be the most stable isomers. Whatever the cluster size (38–260 atoms), the stability order for bare clusters is $\text{Rh}_{\text{core}}\text{Au}_{\text{shell}} > \text{Rh}_{\text{ball}}\text{Au}_{\text{cup}} > \text{Janus} > \text{AuRh}_{\text{ordered}} \approx \text{Au}_{\text{ball}}\text{Rh}_{\text{cup}} > \text{Au}_{\text{core}}\text{Rh}_{\text{shell}}$. Rh adsorbs reactive species such as H_2 , O_2 and CO more strongly than Au and therefore the availability of surface Rh changes the chemisorption properties of Au–Rh nanoalloys. On pure Rh clusters and nanoalloys with neighbouring surface Rh atoms H_2 spontaneously dissociates into H atoms, while the H_2 molecule is elongated (but not broken) for nanoalloys with isolated surface Rh atoms. Similarly, on the Rh part of Au–Rh nanoalloys the dissociation barrier for O_2 almost vanishes. It is also found that the molecular adsorption strength increases on the Rh part of the nanoalloys with respect to pure clusters, although it is not always caused by an upshift of the d-band. The opposite behaviour (to that predicted by the d-band model) has

been observed for adsorption on the Au side of the nanoalloys and the competing nature of strain, alloying and relaxation effects in metal–adsorbate interactions has been demonstrated. It has also been shown that single or multiple Rh atoms bonded to CO or O_2 molecules are thermodynamically more favourable than bare $\text{Rh}_{\text{core}}\text{Au}_{\text{shell}}$, and that core–shell inversion may therefore be induced by the molecular environment. Our segregation results are in agreement with the experimental results of Kiss *et al.*, who observed CO-induced surface segregation of Rh at 300 K for Au–Rh particles grown on TiO_2 surfaces.⁵⁶

It should be noted that the trends described here are based on changes in potential energy rather than in free energy, ignoring entropic effects. The trends in potential energy should give most insight into the behaviour of the considered nanoclusters, though the inclusion of entropy (*e.g.*



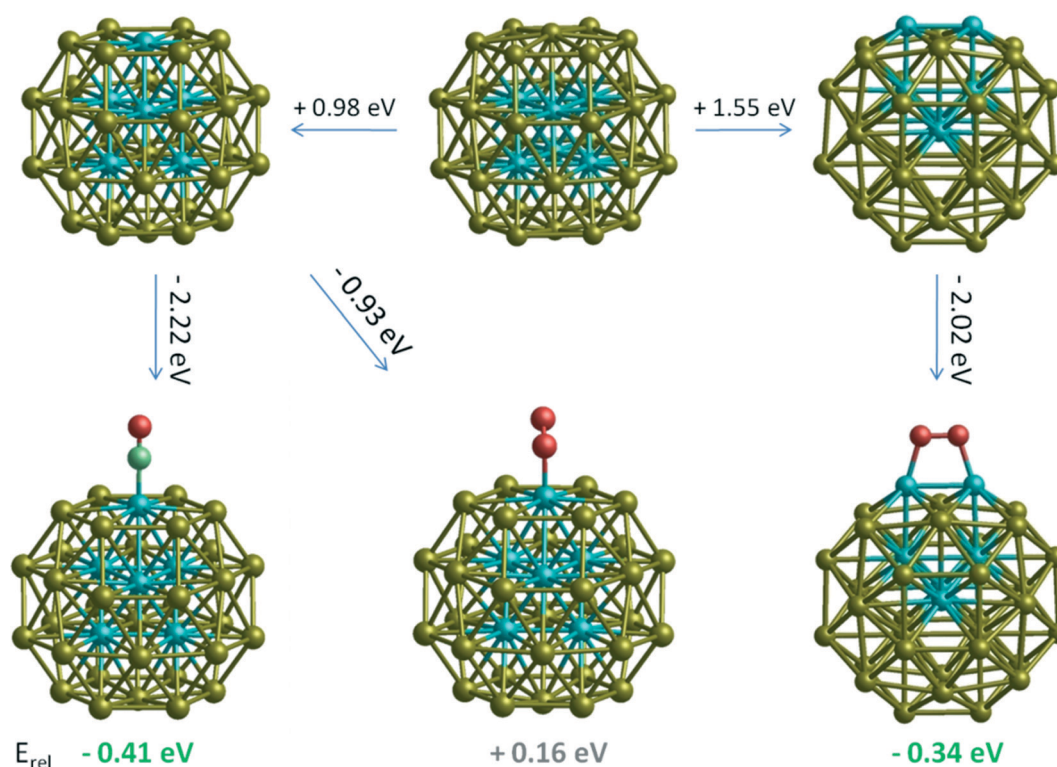


Fig. 11 Energy changes for swapping one or two Rh core atoms with surface gold atoms for the bare $\text{Rh}_{\text{core}}\text{Au}_{\text{shell}}$ cluster and in the presence of adsorbed CO and O_2 . E_{rel} is the energy relative to the $\text{Rh}_{\text{core}}\text{Au}_{\text{shell}}$ cluster, including the adsorbate.

configurational and vibrational entropy) could be investigated *via* DFT-molecular dynamics. Concerning kinetic effects, determination of the energy barriers and the mechanism of adsorbate-induced Rh segregation will be investigated *via* nudged elastic band calculations in future work.

Acknowledgements

This research was funded by the Engineering and Physical Sciences Research Council, UK (EPSRC) under Critical Mass Grant EP/J010804/1 "TOUCAN: Towards an Understanding of Catalysis on Nanoalloys". Calculations were performed on the following HPC facilities: The University of Birmingham BlueBEAR facility (see <http://www.bear.bham.ac.uk/bluebear> for more details) and the UK's national HPC facility, ARCHER, both *via* membership of the UK's HPC Materials Chemistry Consortium, which is funded by EPSRC (EP/L000202), and *via* the TOUCAN grant.

References

- 1 B. Hammer and J. K. Nørskov, *Nature*, 1995, 376, 238–240.
- 2 M. Haruta, T. Kobayashi, H. Sano and N. Yamada, *Chem. Lett.*, 1987, 16, 405–408.
- 3 R. Ferrando, J. Jellinek and R. L. Johnston, *Chem. Rev.*, 2006, 103, 845–910.
- 4 K. J. Andersson, F. Calle-Vallejo, J. Rossmeisl and I. Chorkendorff, *J. Am. Chem. Soc.*, 2009, 131, 2404–2407.
- 5 F. Tao, M. E. Grass, Y. Zhang, D. R. Butcher, J. R. Renzas, Z. Liu, J. Y. Chung, B. S. Mun, M. Salmeron and G. A. Somorjai, *Science*, 2008, 322, 932–934.
- 6 F. Tao, M. E. Grass, Y. Zhang, D. R. Butcher, F. Aksoy, S. Aloni, V. Altoe, S. Alayoglu, J. R. Renzas, C. Tsung, Z. Zhu, Z. Liu, M. Salmeron and G. A. Somorjai, *J. Am. Chem. Soc.*, 2010, 132, 8697–8703.
- 7 P. S. West, R. L. Johnston, G. Barcaro and A. Fortunelli, *J. Phys. Chem. C*, 2010, 114, 19678–19686.
- 8 P. S. West, R. L. Johnston, G. Barcaro and A. Fortunelli, *Eur. Phys. J. D*, 2013, 67, 165.
- 9 L. O. Paz-Borbon, R. L. Johnston, G. Barcaro and A. Fortunelli, *Eur. Phys. J. D*, 2009, 52, 131–134.
- 10 J. Knudsen, A. U. Nilekar, R. T. Vang, J. Schnadt, E. L. Kunkes, J. A. Dumesic, M. Mavrikakis and F. Besenbacher, *J. Am. Chem. Soc.*, 2007, 129, 6485–6490.
- 11 O. M. Lovvik and S. M. Opalka, *Surf. Sci.*, 2008, 602, 2840–2844.
- 12 S. Holloway, B. I. Lundqvist and J. K. Nørskov, *Proceedings of the Eighth Conference on Catalysis*, Berlin, 1984, vol. IV, p. 85.
- 13 B. Hammer and J. K. Nørskov, *Surf. Sci.*, 1995, 343, 211–220.
- 14 A. Ruban, B. Hammer, P. Stoltze, H. Skriver and J. Nørskov, *J. Mol. Catal. A: Chem.*, 1997, 115, 421–429.
- 15 M. Mavrikakis, B. Hammer and J. K. Nørskov, *Phys. Rev. Lett.*, 1998, 81, 2819–2822.



- 16 P. Liu and J. K. Norskov, *Phys. Chem. Chem. Phys.*, 2001, 3, 3814–3818.
- 17 Y. Gauthier, M. Schmid, S. Padovani, E. Lundgren, V. Bus, G. Kresse, J. Redinger and P. Varga, *Phys. Rev. Lett.*, 2001, 87, 036103.
- 18 J. R. Kitchin, J. K. Norskov, M. A. Barteau and J. G. Chen, *J. Chem. Phys.*, 2004, 120, 10240.
- 19 H. Xin and S. Linic, *J. Chem. Phys.*, 2010, 132, 221101.
- 20 Y. Lei, H. Zhao, R. D. Rivas, S. Lee, B. Liu, J. Lu, E. Stach, R. E. Winans, K. W. Chapman, J. P. Greeley, J. T. Miller, P. J. Chupas and J. W. Elam, *J. Am. Chem. Soc.*, 2014, 136, 9320–9326.
- 21 P. C. Jennings, H. A. Aleksandrov, K. M. Neyman and R. L. Johnston, *Nanoscale*, 2014, 6, 1153–1165.
- 22 K. P. McKenna and A. L. Schluger, *J. Phys. Chem. C*, 2007, 111, 18848–18852.
- 23 L. O. Paz-Borbon, R. L. Johnston, G. Barcaro and A. Fortunelli, *Eur. Phys. J. D*, 2009, 52, 131–134.
- 24 N. Austin, J. K. Johnston and G. Mpourmpakis, *J. Phys. Chem. C*, 2015, 119, 18196–18202.
- 25 G. Mpourmpakis, A. N. Andriotis and D. G. Vlachos, *Nano Lett.*, 2010, 10, 1041–1045.
- 26 Y. Yuan, N. Yan and P. J. Dyson, *ACS Catal.*, 2012, 2, 1057–1069.
- 27 R. H. Davies, A. T. Dinsdale, J. A. Gisby, J. A. J. Robinson and S. M. Martin, *CALPHAD: Comput. Coupling Phase Diagrams Thermochem.*, 2002, 26, 229–271.
- 28 S. Garcia, L. Zhang, G. W. Piburn, G. Henkelman and S. M. Humphrey, *ACS Nano*, 2014, 8, 11512–11521.
- 29 Z. Konuspayeva, P. Afanasiev, T. S. Nguyen, L. D. Felice, F. Morfin, N. T. Nguyen, J. Nelayah, C. Ricolleau, Z. Y. Li, J. Yuan, G. Berhault and L. Piccolo, *Phys. Chem. Chem. Phys.*, 2015, 17, 28112–28120.
- 30 R. L. Chantry, W. Siriwatcharapiboon, S. L. Horswell, A. J. Longsdail, R. L. Johnston and Z. Y. Li, *J. Phys. Chem. C*, 2012, 116, 10312–10317.
- 31 R. L. Chantry, I. Atanasov, W. Siriwatcharapiboon, B. P. Khanal, E. R. Zubarev, S. L. Horswell, R. L. Johnston and Z. Y. Li, *Nanoscale*, 2013, 5, 7452–7457.
- 32 R. L. Chantry, I. Atanasov, S. L. Horswell, Z. Y. Li and R. L. Johnston, in *Gold clusters, Colloids, and Nanoparticles II*, ed. D. M. P. Mingos, Structure and Bonding, Springer International Publishing, 2014, vol. 162, pp. 67–90.
- 33 L. Ovari, A. Berko, R. Gubo, A. Racz and Z. Konya, *J. Phys. Chem. C*, 2014, 118, 12340–12352.
- 34 E. R. Essinger-Hileman, D. DeCicco, J. F. Bondi and R. E. Schaak, *J. Mater. Chem.*, 2011, 21, 11599–11604.
- 35 T. S. Nguyen, D. Laurenti, Z. Konuspayeva, P. Afanasiev and L. Piccolo, in preparation.
- 36 L. O. Paz-Borbon, A. Gupta and R. L. Johnston, *J. Mater. Chem.*, 2008, 18, 4154–4164.
- 37 G. Kresse and J. Hafner, *Phys. Rev. B: Condens. Matter*, 1993, 47, 558–561.
- 38 J. P. Perdew, K. Burke and M. Ernzerhof, *Phys. Rev. Lett.*, 1996, 77, 3865–3868.
- 39 P. E. Blöchl, *Phys. Rev. B: Condens. Matter*, 1994, 50, 17953–17979.
- 40 G. Kresse and D. Joubert, *Phys. Rev. B: Condens. Matter*, 1999, 59, 1758–1775.
- 41 G. Mills, H. Jonsson and G. K. Schenter, *Surf. Sci.*, 1995, 324, 305–337.
- 42 H. Jonsson, G. Mills and K. W. Jacobsen, Nudged elastic band method for finding minimum energy paths of transitions, in *Classical and Quantum Dynamics in Condensed Phase Simulations*, ed. B. J. Berne, G. Ciccotti and D. F. Coker, World Scientific, Singapore, 1998, p. 385.
- 43 R. Ferrando, A. Fortunelli and G. Rossi, *Phys. Rev. B: Condens. Matter Mater. Phys.*, 2005, 72, 085449.
- 44 P. Ferrin, S. Kandoi, A. U. Nilekar and M. Mavrikakis, *Surf. Sci.*, 2012, 606, 679–689.
- 45 M. Okumura, Y. Kitagawa, M. Haruta and K. Yamaguchi, *Appl. Catal., A*, 2005, 291, 37–44.
- 46 L. Barrio, P. Liu, J. A. Rodriguez, J. M. Campos-Martin and J. L. G. Fierro, *J. Chem. Phys.*, 2006, 125, 164715.
- 47 A. A. Peterson, L. C. Grabow, T. P. Brennan, B. Shong, C. Ooi, D. M. Wu, C. W. Li, A. Kushwaha, A. J. Medford, F. Mbuga, L. Li and J. K. Norskov, *Top. Catal.*, 2012, 55, 1276–1282.
- 48 J. J. Pireaux, M. Chtaib, J. P. Delrue, P. A. Thiry, M. Liehr and R. Caudano, *Surf. Sci.*, 1984, 141, 211–220.
- 49 C. Comelli, V. R. Dhanak, M. Kiskinova, K. C. Price and P. Rose, *Surf. Sci. Rep.*, 1998, 32, 165–231.
- 50 Y. Xu and M. Mavrikakis, *J. Phys. Chem. B*, 2003, 107, 9298–9307.
- 51 B. E. Salisbury, W. T. Wallace and P. L. Whetten, *Chem. Phys.*, 2000, 262, 131–141.
- 52 A. Roldan, J. M. Ricard and F. Illas, *Theor. Chem. Acc.*, 2011, 128, 675–681.
- 53 L. Piccolo, D. Loffreda, F. J. Cadete Santos Aires, C. Deranlot, Y. Jugnet, P. Sautet and J. C. Bertolini, *Surf. Sci.*, 2004, 566–568, 995–1000.
- 54 J. Wang, M. McEntee, W. Tang, M. Neurock, A. P. Baddorf, P. Maksymovych and J. T. Yates, *J. Am. Chem. Soc.*, 2016, 138, 1518–1526.
- 55 L. Vitos, A. V. Ruban, H. L. Skriver and J. Kollar, *Surf. Sci.*, 1998, 411, 186–202.
- 56 J. Kiss, L. Ovari, A. Oszko, G. Potari, M. Toth, K. Baan and A. Erdohelyi, *Catal. Today*, 2012, 181, 163–170.

